GSA TODAY

THE GEOLOGICAL SOCIETY
OF AMERICA®

A High-Resolution Multispectral Macro-Imager for Geology and Paleontology

A High-Resolution Multispectral Macro-Imager for Geology and Paleontology

Ryan A. Manzuk, *Dept. of Geosciences, Princeton University, Princeton, New Jersey 08544, USA, rmanzuk@princeton.edu;* **Devdigvijay Singh,** *Dept. of Geosciences, Princeton University, Princeton, New Jersey 08544, USA;* **Akshay Mehra,** *Dept. of Geosciences, Princeton University, Princeton, New Jersey 08544, USA, and Dept. of Earth Sciences, Dartmouth College, Hanover, New Hampshire 03755, USA;* **Emily C. Geyman,** *Dept. of Geosciences, Princeton University, Princeton, New Jersey 08544, USA, and Division of Geological and Planetary Sciences, California Institute of Technology, Pasadena, California 91125, USA;* **Stacey Edmonsond,** *Dept. of Geosciences, Princeton University, Princeton, New Jersey 08544, USA, and School of Earth and Ocean Sciences, University of Victoria, Victoria, British Columbia V8W 2Y2, Canada;* **Adam C. Maloof,** *Dept. of Geosciences, Princeton University, Princeton, New Jersey 08544, USA*

ABSTRACT

Accurately assessing the shape, size, and modality of features in rock samples is a longstanding problem in geology. Recent advances in machine learning have introduced the possibility of performing these tasks through automated image analysis. To leverage these methods for geological and paleontological applications, we first need a way to acquire high-resolution images of polished slabs and thin sections with a field of view large enough to fit samples containing crystals, fossils, bedforms, etc. We describe a new multispectral setup that can acquire images at ~3.76 mm per pixel spatial resolution over a 21 cm^2 field of view, equipped with 8-band (470–940 nm) spectral resolution, plus a band for ultraviolet (365 nm) fluorescence. Additionally, we present a 5-band (470–940 nm) light table with automated rotating polarizers, which allows use of the camera as a high-throughput transmitted light thin section imager. The use of color bands outside the visible spectrum, as well as the registration of multiple cross-polarized rotations, encode rock properties that heighten image contrast and improve the accuracy of machine learning models. Our setup and methods provide an efficient way to (1) build reproducible image archives of rock specimens to complement field observations, (2) classify and segment those images, and (3) quantitatively compare lithofacies and fossil assemblages.

INTRODUCTION

Geologists have developed an eye for the physical rock characteristics that encode Earth's sedimentary, igneous, and meta- morphic history. At points on a map or beds in a stratigraphic section, lithofacies obser- vations from field campaigns form the backbone of geologic study. Throughout recent decades, the rise of geochemical techniques has increased the value of sam- ples brought back from the field. For exam- ple, many measured sections through car- bonate stratigraphies now include bed-by-bed isotope and trace element measurements that give insights into local carbon cycling (Ahm et al., 2021), global marine redox state (Dahl et al., 2019), sediment diagene- sis (Ahm et al., 2018), and correlations within (Hay et al., 2019) and between basins (Halverson et al., 2005; Maloof et al., 2010). However, reliable interpretations of these geochemical data benefit from knowledge of the physical properties of the rock sam- ples, such as grain/crystal sizes and modal- ities (Geyman and Maloof, 2021), primary mineralogy, porosity/permeability, and cross-cutting relationships between fabrics (Bergmann et al., 2011; Hood et al., 2016; Corsetti et al., 2006; Dyer et al., 2017)— data that also serve to refine analyses of sedimentary environment (Geyman et al., 2021). The above examples come from sedi- mentary geology, but the need to match geochemical data to quantitative lithofacies also applies to interpretations of igneous and metamorphic conditions (Higgins, 2000).

Workers have developed methods to approximate rock contents from samples, often by point counting on the stage of a microscope (Shand, 1916). Although this technique has brought about many geologi- cal insights, the uncertainties that stem from incompletely sampling a rock's surface are significant (Solomon, 1963; Neilson and Brockman, 1977), and the small fields of view available in most microscopes limit the scale of features studied to those only a few millimeters in size (Higgins, 2000). To build on previous petrographic findings and contextualize geochemical data, we can develop techniques to quantify lithofacies over a broader range of feature sizes and with more continuous spatial sampling.

New Potential for Petrographic Data through Image Analysis

Geologists could outline, count, and mea- sure all the fossils, grains, or crystals in sam- ples to extract these data, but manual petro- graphic study is too time-consuming to accompany each of the hundreds or thou- sands of geochemical measurements and observations made on a single map. We can, however, turn to recent advances in machine learning that have introduced the possibility of training models to recognize rock fea- tures (Yesiloglu-Gultekin et al., 2012; Koeshidayatullah et al., 2020). The need for automated feature classification is familiar to many fields, and effective solutions now are being realized in industries such as autonomous vehicles (Tian et al., 2018) and biomedical image processing (Li et al., 2018).

A variety of machine learning models can be trained to perform these tasks, but they all learn to classify image features through repeated practice on example images manually labeled by humans (LeCun et al., 1989), and some of the most effective mod- els for general applications require more than 300,000 traced examples (Lin et al., 2014; He et al., 2017). Prior to training an

equivalent model to recognize rock features, we first need to think about the properties of the images themselves and how well they capture those features. A potential advantage for automated classification of rock elements is that geological materials are made up of minerals with distinctive reflectance (Bishop et al., 2019) and birefringence (Cesare et al., 2022) characteristics. Capturing these spectral properties with a camera sensitive to more color bands than the human eye can heighten contrast between features in images and reduce the number of training examples needed for accurate classification models (Soomro et al., 2017). Here, we introduce a multispectral camera optimized for petrographic study, which can facilitate image analysis as a laboratory method to complement other geochemical and geophysical measurements.

IMAGING SETUP

The imaging setup presented herein is a modification of the grinding, imaging, and reconstruction instrument (GIRI), housed at Princeton University (Mehra and Maloof, 2018). While GIRI is a specialized solution for either two- or three-dimensional imaging, a similar imaging setup could be realized independent of GIRI with widely available cameras and lights.

Field of View and Spatial Resolution

There is a trade-off between field of view (FOV) and spatial resolution, and so a camera for geological samples must balance these two variables to capture a broad size range of rock features. For many geological applications, pixels on the order of 5 µm are needed to maintain sharp grain boundaries. Most current camera attachments for petrographic or dissecting microscopes achieve this resolution or greater, but only with FOVs smaller than 1 cm², which limits feature sizes and can add uncertainty to modality data.

To maintain high spatial resolution while expanding FOV, we design our camera around the continually improving technologies of optical sensors and macro lenses. Our camera sensor is a Phase One IQ4 150-megapixel digital back (Fig. 1D), which measures 4.04 × 5.37 cm with 3.76 µm pixels. We use a 120 mm Schneider Kreuznach apochromatic macro lens, which enables 1:1 photography with an FOV and pixel resolution equal to the dimensions of the digital back. Other lenses can be substituted to increase FOV at the cost of per-pixel
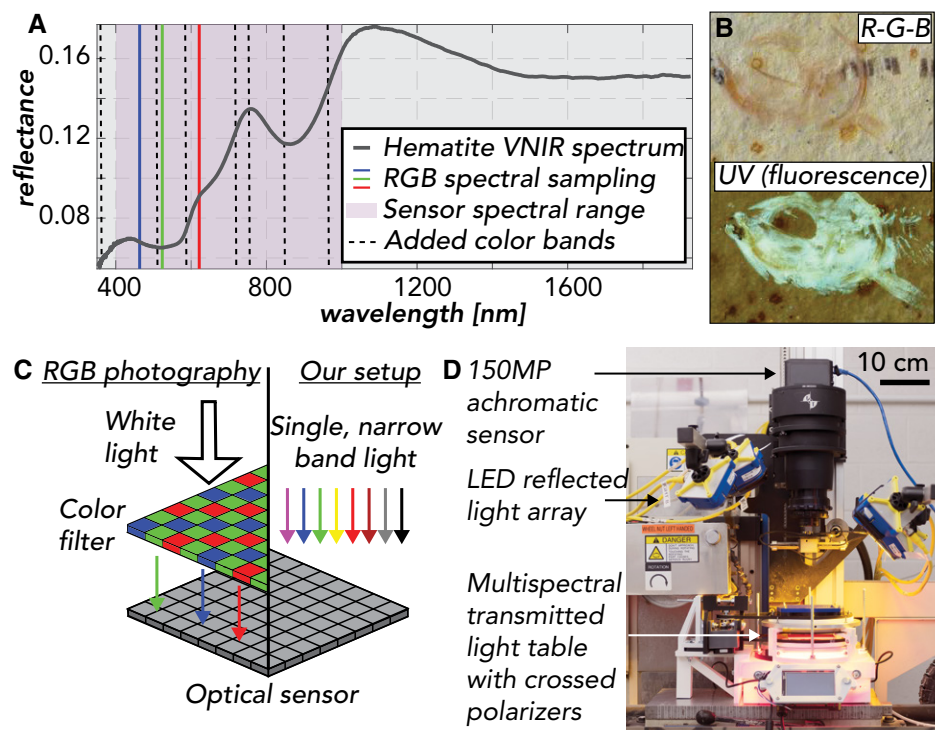
Figure 1. Motivating principles and setups for multispectral petrographic imaging with both reflected and transmitted light. (A) The addition of bands within the sensitivity range of a standard optical sensor allows for the sampling of distinctive spectral characteristics, such as the hematite peak and trough near 750 nm and 850 nm, respectively. (B) Ultraviolet (UV) fluorescence is an informative source of contrast when studying materials responsive to UV light, like the apatitic and organic components of this fish fossil (from Tischlinger and Arratia, 2013). (C) Traditional cameras filter incoming light to just red, green, and blue signals, limiting spectral range and reducing the spatial resolution of each color. We use narrowband lights (one at a time), which allows us to capture signals from the full range of sensitivity, and at the full resolution of the optical sensor. (D) Photograph of our setup. RGB—red-green-blue; VNIR—visible to near-infrared.

resolution. To reduce glare and improve image contrast, we place a broadband polarizer over the lens.

Spectral Resolution

One of the key lessons learned from 50 years of satellite-based remote sensing of Earth's surface is the utility of bands outside the traditional red-green-blue (RGB) visible spectrum to take advantage of the unique reflective characteristics of rocks and vegetation (Melesse et al., 2007). The reflective properties of certain geological materials in the visible to near-infrared (VNIR; 300–1100 nm) spectrum still apply at the scale of a hand sample and can be used by a petrographic camera to maximize feature contrast and aid segmentation.

Increasing the range and number of light spectra imaged usually diminishes spatial resolution because increasingly long wavelength (>1000 nm) and/or narrowband light sources are low intensity, meaning cameras designed for hyperspectral imaging must have larger pixels to gather enough photons to form a signal. Thus, we cannot design an

imager with continuous spectral coverage throughout the VNIR spectrum and instead choose to optimize for the trade-off between spatial and spectral resolution (Ma et al., 2014). Our optical sensor (sensitive from 300 to 1000 nm) maintains the highest available spatial resolutions while still detecting important spectral properties beyond RGB. In particular, metallic oxides, clay minerals, pyroxenes, and olivines have absorption bands at wavelengths less than 1000 nm that can enhance contrast between geological classes (Bishop et al., 2019; Fig. 1A).

We create color channels by illuminating samples with an array of eight Smart Vision S75 narrowband LEDs (Fig. 1D), which can be chosen from any of the ten wavelengths shown in Figure 1A. We inform our selection of lights through preliminary tests for maximized feature contrast and equip all lights with a polarizing film to reduce glare.

Ultraviolet (UV) Fluorescence

In a dark laboratory setting, fluorescence from minerals like carbonates and phosphates can add contrast when imaged in the visible

spectrum. For example, in carbonate rocks at successive stages of calcite precipitation, diagenesis, and recrystallization, differences in the trace element chemistry of the stages will produce heterogeneities in the strength of fluorescence and thus contrast in the image (Dravis and Yurewicz, 1985). Additionally, organic or apatitic fossil materials often fluoresce, making UV fluorescence photography a valuable tool for creating contrast in paleontological samples (Tischlinger and Arratia, 2013; Fig. 1B). To image fluorescence, we illuminate samples with a 365 nm SmartVision LED. To reduce noise in the images, we place a bandpass filter with a cut-off wavelength of 395 nm over the UV light to remove any visible components of the emitted spectrum and use a 400 nm cut-on UV filter in front of the lens to eliminate any UV light from reaching the camera sensor. Note that when imaging with UV, the camera records the fluorescence of the materials in the VNIR spectrum.

Transmitted Light

Thin section transmitted light imagery offers another opportunity for increased contrast. Anisotropy, cleavage, and twinning create distinctive qualities in grains and crystals within a thin section and delineate grain boundaries (Rogers and Kerr, 1942). Additionally, crossed polarizers in transmitted light setups heighten contrast between features by creating differential extinction and birefringence patterns (Rogers and Kerr, 1942). To image thin sections with transmitted plane-polarized (PPL) and cross-polarized (XPL) light, we have created a light table that can be used with GIRI or any camera stand setup (Fig. 1D). The light source for this table is a dense Ramona Optics LED board with five wavelengths (470, 530, 620, 850, 940 nm), which illuminates the sample through a diffuser and a broadband linear polarizer. To image XPL, we attach a second polarizer over the sample, perpendicular to the lower linear polarizer (Fig. 1D). Unlike traditional petrographic microscopes, this light table holds the sample fixed, while a NEMA 17 stepper motor rotates both polarizers synchronously (Fueten, 1997) with a precision of 2.8×10^{-4} degrees.

Data Processing

In the case of both transmitted and reflected light, all captured image channels are perfectly aligned, allowing the user to view any three channels in a false color image or analyze all captures as a single multichannel image. Our setup, like all cameras, contends with chromatic aberration, whereby each wavelength of light achieves maximal sharpness at a different focal depth due to the wavelength-dependence of light refraction (Jacobson et al., 2013). In the supplemental material[1], we demonstrate how we apply blur modeling and deconvolution to achieve multispectral images that are sharper than a standard RGB camera.

RESULTS

In the following case studies, we illustrate two examples where the added spectral data from our reflected and transmitted light setups enhance our ability to distinguish features within geological samples. To classify pixels, we use a support vector machine (SVM), which is a simple machine learning model, to show the potential for future machine learning efforts when trained on these more informative spectral data.

Case Study 1: Feature Mapping in Reflected Light

A lack of contrast between classes in reflected light imagery commonly stems from all pixel values falling near a brightness line—a 1:1 intensity line where values are well-correlated between channels (Fig. 2B). In Figure 2A, we show an RGB image of an
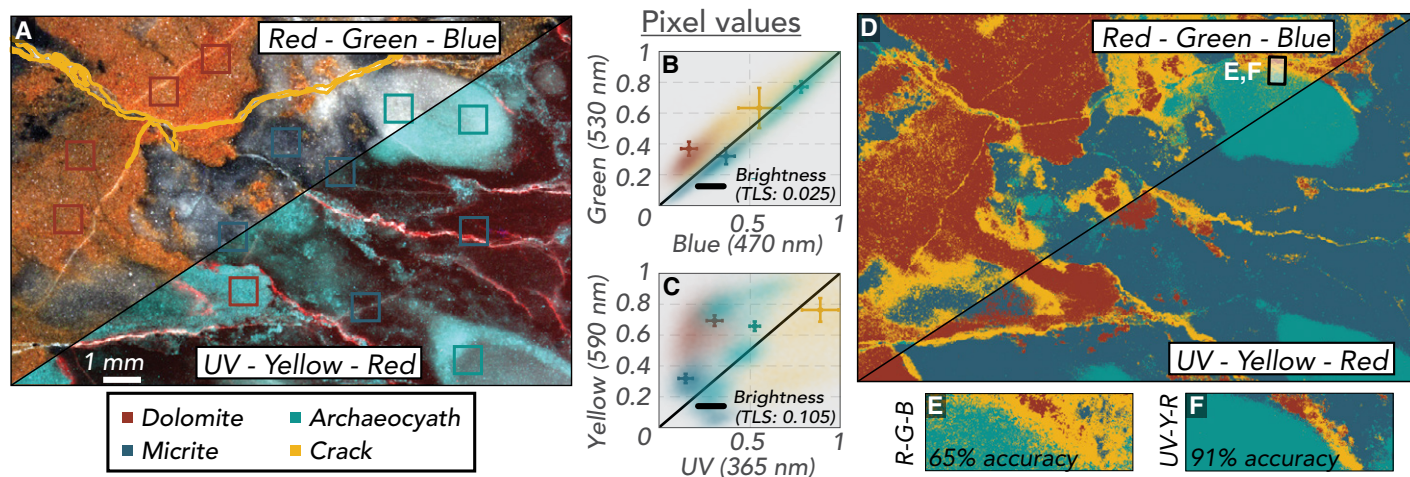

Figure 2. Improved segmentation results with multispectral reflected light imagery. (A) We take the same image of an archaeocyathid boundstone sample in a traditional red-green-blue (RGB) colorspace, as well as a false color ultraviolet (UV)-yellow-red space and sample the same pixels for four feature classes in each (colored boxes). (B) In the RGB image, all classes show covariance between color channels, and most pixels fall around the brightness line. (C) In the UV-yellow-red (UV-Y-R) image, covariance between channels is removed for all classes, as evidenced by the fourfold increase in average distance between each pixel and the brightness line (reported as total least squares, TLS). The movement of all classes away from the brightness line into distinct regions of the color space eases segmentation. (D–F) Using a support vector machine (SVM), an automated classification of the RGB image is 65% accurate and does not give high-resolution borders between classes and regions (D, E). In contrast, an SVM segmentation of the UV-yellow-red image is 91% accurate and gives sharp region and class boundaries more suitable for measurements (D, F).

archaeocyathid boundstone sample, wherein each of the four classes (dolomite, micritic calcite, archaeocyathid, and calcite-filled crack) shows well-correlated pixel values (Fig. 2B). When segmenting these samples, the class overlap in RGB space hinders pixel-wise classification, leading to uncertain boundaries between classes (Figs. 2D and 2E). The same image in a UV-yellow-red colorspace (Fig. 2A) shows reduced channel covariance for all four classes (Fig. 2C). With the new spectral information available in UV-yellow-red space, an SVM has 30% improved accuracy, and produces resolved regions with distinct boundaries for each class (Figs. 2D and 2F).

Case Study 2: Feature Mapping in Transmitted Light

A primary limitation of performing image analysis on thin sections with existing microscope cameras is the FOV. In this example, we use a granite sample from the Golden Horn Batholith (Eddy et al., 2016) that has crystals with diameters approaching 1 cm.

Because these crystals are large relative to a microscope FOV (Fig. 3A), the concentration of minerals in an image will be variable depending on the portion of the thin section placed under the lens. For example, the concentration of plagioclase assessed through classification may range from 29% to 55% when using the 2.5× objective on a petrographic microscope (Fig. 3H). The variation in concentrations increases if magnification increases (reducing FOV) or point counts are used to assess modality as opposed to pixel classifications (Fig. 3H).

This example also illustrates the benefit of building additional image channels from polarizer orientations (as opposed to additional wavelengths of light). With a single RGB image from one orientation of the crossed polarizers, capturing all possible birefringence and extinction properties for a given mineral class in a training set can be difficult and time-consuming, and the end result can be inaccurate classification (Fig. 3F). When multiple rotation XPL images are stacked together in the training set, each

pixel takes on a broader range of the color and textural properties that a mineral may exhibit in cross-polarized light, which helps the machine learning model generalize and leads to more accurate classifications with the same number of training samples (Figs. 3C, 3D, and 3G).

DISCUSSION

Because our camera improves outcomes when using machine learning techniques to produce petrographic data, we now are focused on high-throughput methods for complete sample image analyses within stratigraphic sections or geologic maps. Our workflow takes the same samples gathered for geochemical or geophysical laboratory analyses and photographs them as polished slabs and/or thin sections. As an example, we created a bed-by-bed library containing nearly 2,000 images that chronicles paleoenvironmental change through the lower Ordovician Kinblade Formation (Fig. 4). Within a single map or section, systematic image analysis can yield lithofacies
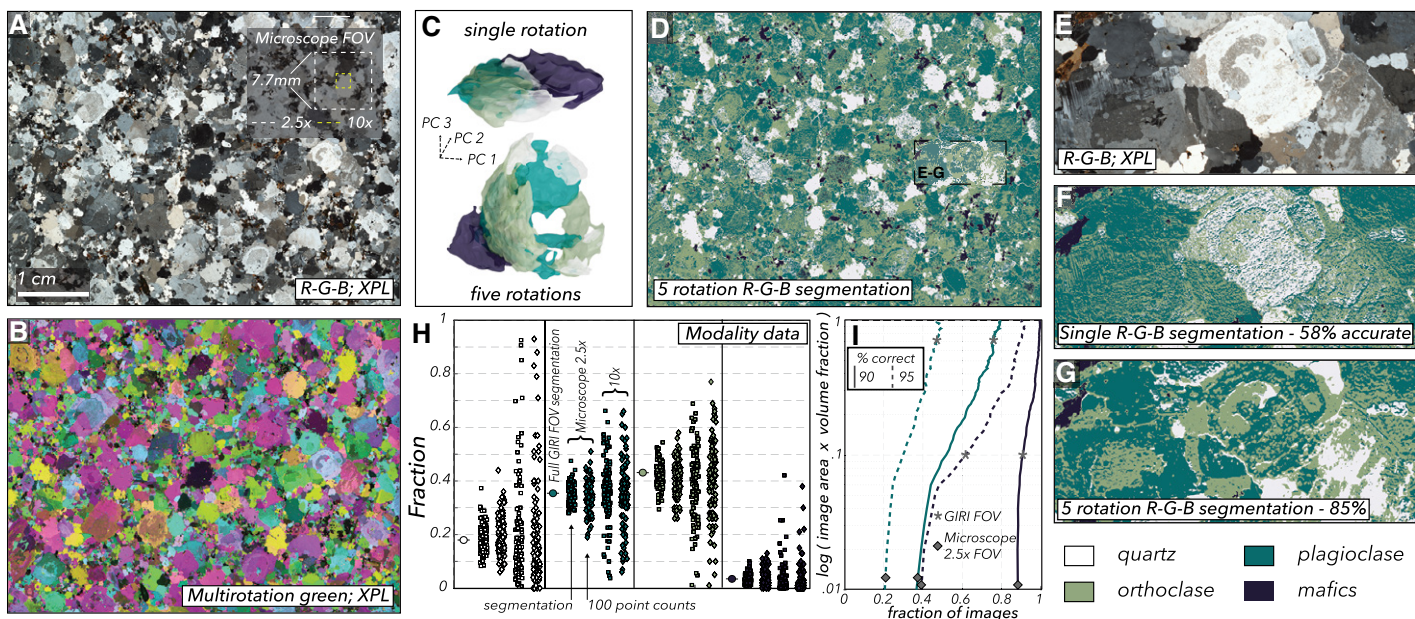

Figure 3. Improved modality data from multiple rotations of crossed polarizers for transmitted light imagery of thin sections. (A) Red-green-blue (RGB), cross-polarized (XPL) image of a granite thin section from the Golden Horn Batholith showing the full field of view (FOV) possible with our setup compared to those obtainable with a microscope camera. (B) False color image obtained using green (530 nm) light at three separate XPL orientations, 18° apart. (C) In principal component (PC) space, the pixel values for the four mineral classes (quartz, plagioclase, orthoclase, and mafics) in a single rotation RGB XPL image mostly overlap in one area of the plot. For an RGB XPL image containing five 18° rotations stacked into a 15-channel image, the pixel values spread out into a cone, where the position on the cone occupied by a given pixel relates to the class of the mineral and the relative orientation of its crystallographic axis. This added separation of the classes in the PC space of the five rotation XPL image improves the accuracy of pixel classifications from machine learning models, like the example given in (D). (E–G) In a zoomed-in portion of the image (E), we see that a support vector machine (SVM) using just a single rotation XPL RGB image (F) is 27% less accurate at classifying pixels compared to an SVM that is given the five-rotation image (G). Even with accurate classifications, analyzing only a relatively small FOV can add uncertainty. We see in (H) that the resulting modality data from the classification in (C) have highly variable values when assessed within the FOV of a traditional petrographic microscope. Each point in the plot represents the modality assessed in a randomly selected area of the segmentation equal to the size of a microscope FOV using either a 2.5× or 10× objective. The variation in these errors between classes stems from the characteristic size and relative abundance of the minerals. (I) To show the effect of crystal size and abundance, we calculate the number of images that correctly estimate the modality of a given mineral in a view size normalized to the mineral abundance (determined using a 4.5 × 5.5 × 4 cm 3D grinding, imaging, and reconstruction instrument [GIRI] reconstruction of the sample). In an experiment randomly drawing thin sections from the full volume of this granite sample, we see that an approximately equal fraction of images estimates the mafic mineral modality within a 90% correctness threshold when comparing GIRI to a 2.5× microscope objective. However, at the 95% threshold, as well as with the larger plagioclase crystals, the GIRI FOV performs nearly twice as well.
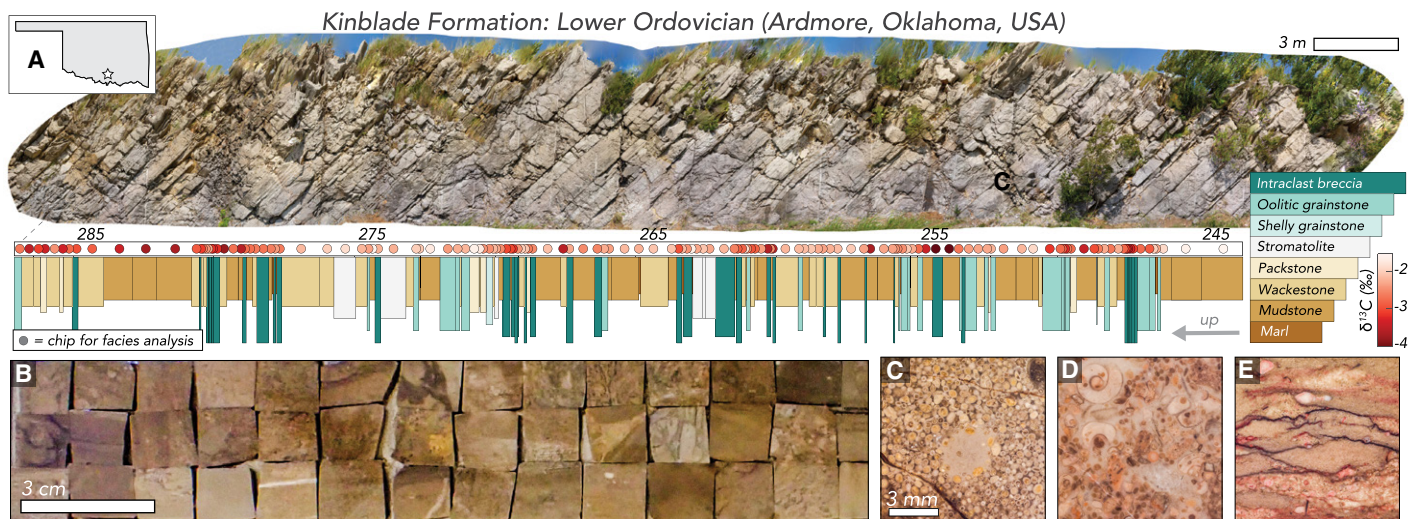
Figure 4. Example of a reproducible, quantitative lithofacies data set. (A) The lower Ordovician Kinblade Formation outcropping in Ardmore Oklahoma (GPS location: 34.372821, −97.145353) is a 791 m succession of carbonate strata containing 1,922 beds. (B) Following bed-by-bed field study, sampling, and geochemical measurement, we epoxy 1 cm² chips from each sample for efficient grinding, polishing, and imaging. The chip size is chosen to best encapsulate the dominant grain, fossil, and bedform sizes in the data set. The resulting ~2,000 images (examples C–E, shown here in red-green-blue space, but all are 8-channel multispectral images) now are a documentation of the lithofacies in the measured section at Ardmore and ready for image analysis, classification, segmentation, and interpretation.

data that quantify spatio-temporal patterns in grain, crystal, and fossil characteristics, while allowing new tests of geochemical interpretations (e.g., Geyman and Maloof, 2021; Ahm et al., 2019).

At the same time, amassing a standardized, multispectral image library with annotated examples (Deng et al., 2009) of geologic features from many localities will help train more general machine learning models for petrography. These collections of slab and thin-section images are a first step toward the goal of automated routines to measure features in rock samples from pictures. Curated image libraries also can serve as a classroom tool for teaching petrography, and student work to classify images can provide training examples for machine learning—a crowdsourcing technique that has seen recent success in several fields (e.g., van den Bergh et al., 2021).

In addition to improving lithofacies data, we see our camera and petrographic images as a vehicle to improve access and reproducibility in geology. Open access to archives like Integrated Ocean Drilling Program (IODP) cores has expanded the number of people producing complementary data sets and provided for deeper, more reproducible studies of Earth's climate and oceans in recent geologic periods (Becker et al., 2019). A similar framework should exist for rock outcrops that span deeper into Earth's history, where, currently, the observations that form geologic maps and stratigraphic sections

tend to be documented primarily in field notes or illustrative outcrop/sample photographs. For corroboration or expansion upon previous outcrop-based studies, this system requires workers to visit the locality themselves. Instead, open access to standardized petrographic image collections will allow broader groups of researchers to measure and interpret features in rock formations from around the world, enhancing both reproducibility (Baker, 2016) and diversity, equity, and inclusion (Fernandes et al., 2020) in geology. Although our archives are not continuous records like IODP cores, they benefit from the added spatial context available at rock outcrops and provide a zoomed-in perspective to supplement constantly improving aerial survey techniques (Shah et al., 2021). In concert with satellite, drone-derived, and hand-held imagery, our pipeline for systematic imaging, classification, and measurement of rock samples can form an important layer in multiscale digitization and interpretation of physical rock properties.

sions. We also appreciate the constructive feedback received from reviewer Sarah Jacquet and editor James Schmitt.

REFERENCES CITED

Ahm, A.S.C., Bjerrum, C.J., Blättler, C.L., Swart, P.K., and Higgins, J.A., 2018, Quantifying early marine diagenesis in shallow-water carbonate sediments: Geochimica et Cosmochimica Acta, v. 236, p. 140–159, https://doi.org/10.1016/j.gca.2018.02.042.

Ahm, A.S.C., Maloof, A.C., Macdonald, F.A., Hoffman, P.F., Bjerrum, C.J., Bold, U., Rose, C.V., Strauss, J.V., and Higgins, J.A., 2019, An early diagenetic deglacial origin for basal Ediacaran "cap dolostones": Earth and Planetary Science Letters, v. 506, p. 292–307, https://doi.org/10.1016/j.epsl.2018.10.046.

Ahm, A.S.C., Bjerrum, C.J., Hoffman, P.F., Macdonald, F.A., Maloof, A.C., Rose, C.V., Strauss, J.V., and Higgins, J.A., 2021, The Ca and Mg isotope record of the Cryogenian Trezona carbon isotope excursion: Earth and Planetary Science Letters, v. 568, 117002, https://doi.org/10.1016/j.epsl.2021.117002.

Baker, M., 2016, Reproducibility crisis: Nature, v. 533, p. 353–366.

Becker, K., Austin, J.A., Exon, N., Humphris, S., Kastner, M., McKenzie, J.A., Miller, K.G., Suyehiro, K., and Taira, A., 2019, 50 Years of Scientific Ocean Drilling: Oceanography (Washington, D.C.), v. 32, p. 17–21, https://doi.org/10.5670/oceanog.2019.110.

Bergmann, K.D., Zentmyer, R.A., and Fischer, W.W., 2011, The stratigraphic expression of a large negative carbon isotope excursion from the Ediacaran Johnnie Formation, Death Valley: Precambrian Research, v. 188, p. 45–56, https://doi.org/10.1016/j.precamres.2011.03.014.

Bishop, J.L., Bell, J.F., III, and Moersch, J.E., editors, 2019, Remote Compositional Analysis:

Techniques for Understanding Spectroscopy, Mineralogy, and Geochemistry of Planetary Surfaces. Volume 24: Cambridge, UK, Cambridge University Press, https://doi.org/10.1017/9781316888872.

Cesare, B., Campomenosi, N., and Shribak, M., 2022, Polychromatic polarization: Boosting the capabilities of the good old petrographic microscope: Geology, v. 50, p. 137–141, https://doi.org/10.1130/G49303.1.

Corsetti, F.A., Kidder, D.L., and Marenco, P.J., 2006, Trends in oolite dolomitization across the Neoproterozoic-Cambrian boundary: A case study from Death Valley, California: Sedimentary Geology, v. 191, p. 135–150, https://doi.org/10.1016/j.sedgeo.2006.03.021.

Dahl, T.W., Connelly, J.N., Li, D., Kouchinsky, A., Gill, B.C., Porter, S., Maloof, A.C., and Bizzarro, M., 2019, Atmosphere-ocean oxygen and productivity dynamics during early animal radiations: Proceedings of the National Academy of Sciences of the United States of America, v. 116, p. 19,352–19,361, https://doi.org/10.1073/pnas.1901178116.

Deng, J., Dong, W., Socher, R., Li, L.J., Li, K., and Fei-Fei, L., 2009, Imagenet: A large-scale hierarchical image database: 2009 IEEE Conference on Computer Vision and Pattern Recognition: IEEE, p. 248–255, https://10.1109/CVPR.2009.5206848.

Dravis, J.J., and Yurewicz, D.A., 1985, Enhanced carbonate petrography using fluorescence microscopy: Journal of Sedimentary Research, v. 55, p. 795–804.

Dyer, B., Higgins, J.A., and Maloof, A.C., 2017, A probabilistic analysis of meteorically altered $\delta^{13}C$ chemostratigraphy from late Paleozoic ice age carbonate platforms: Geology, v. 45, p. 135–138, https://doi.org/10.1130/G38513.1.

Eddy, M.P., Bowring, S.A., Miller, R.B., and Tepper, J.H., 2016, Rapid assembly and crystallization of a fossil large-volume silicic magma chamber: Geology, v. 44, p. 331–334, https://doi.org/10.1130/G37631.1.

Fernandes, A.M., Abeyta, A., Mahon, R.C., Martindale, R., Bergmann, K.D., Jackson, C., Present, T.M., Swanson, T., Reano, D., Butler, K., Swanson, T., Butler, K., Brisson, S., Johnson, C., Mohrig, D., and Blum, M.D., 2020, "Enriching Lives within Sedimentary Geology": Actionable Recommendations for Making SEPM a Diverse, Equitable and Inclusive Society for All Sedimentary Geologists: EarthArXiv, https://doi.org/10.31223/osf.io/y7v9e.

Fueten, F., 1997, A computer-controlled rotating polarizer stage for the petrographic microscope: Computers & Geosciences, v. 23, p. 203–208, https://doi.org/10.1016/S0098-3004(97)85443-X.

Geyman, E.C., and Maloof, A.C., 2021, Facies control on carbonate $\delta^{13}C$ on the Great Bahama Bank: Geology, v. 49, p. 1049–1054, https://doi.org/10.1130/G48862.1.

Geyman, E.C., Maloof, A.C., and Dyer, B., 2021, How is sea level change encoded in carbonate stratigraphy?: Earth and Planetary Science Letters, v. 560, 116790, https://doi.org/10.1016/j.epsl.2021.116790.

Halverson, G.P., Hoffman, P.F., Schrag, D.P., Maloof, A.C., and Rice, A.H.N., 2005, Toward a Neoproterozoic composite carbon-isotope record: Geological Society of America Bulletin, v. 117, p. 1181–1207, https://doi.org/10.1130/B25630.1.

Hay, C.C., Creveling, J.R., Hagen, C.J., Maloof, A.C., and Huybers, P., 2019, A library of early Cambrian chemostratigraphic correlations from a reproducible algorithm: Geology, v. 47, p. 457–460, https://doi.org/10.1130/G46019.1.

He, K., Gkioxari, G., Dollár, P., and Girshick, R., 2017, Mask R-CNN: Proceedings of the 2017 IEEE International Conference on Computer Vision, p. 2961–2969, https://doi.org/10.1109/ICCV.2017.322.

Higgins, M.D., 2000, Measurement of crystal size distributions: The American Mineralogist, v. 85, p. 1105–1116, https://doi.org/10.2138/am-2000-8-901.

Hood, A.v., Planavsky, N.J., Wallace, M.W., Wang, X., Bellefroid, E.J., Gueguen, B., and Cole, D.B., 2016, Integrated geochemical-petrographic insights from component-selective ^{238}U of Cryogenian marine carbonates: Geology, v. 44, p. 935–938, https://doi.org/10.1130/G38533.1.

Jacobson, R., Ray, S., Attridge, G.G., and Axford, N., 2013, Manual of Photography: New York, Routledge, 464 p., https://doi.org/10.4324/9780080510965.

Koeshidayatullah, A., Morsilli, M., Lehrmann, D.J., Al-Ramadan, K., and Payne, J.L., 2020, Fully automated carbonate petrography using deep convolutional neural networks: Marine and Petroleum Geology, v. 122, 104687, https://doi.org/10.1016/j.marpetgeo.2020.104687.

LeCun, Y., Boser, B., Denker, J., Henderson, D., Howard, R., Hubbard, W., and Jackel, L., 1989, Handwritten digit recognition with a back-propagation network: Advances in Neural Information Processing Systems, v. , p. 396–404.

Li, X., Chen, H., Qi, X., Dou, Q., Fu, C.W., and Heng, P.A., 2018, H-DenseUNet: Hybrid densely connected UNet for liver and tumor segmentation from CT volumes: IEEE Transactions on Medical Imaging, v. 37, p. 2663–2674, https://doi.org/10.1109/TMI.2018.2845918.

Lin, T.Y., Maire, M., Belongie, S., Hays, J., Perona, P., Ramanan, D., Dollár, P., and Zitnick, C.L., 2014, Microsoft COCO: Common objects in context, in Fleet, D., Pajdla, T., Schiele, B., and Tuytelaars, T., eds., Computer Vision—ECCV 2014: Lecture Notes in Computer Science: Berlin, Springer, v. 8693, p. 740–755, https://doi.org/10.1007/978-3-319-10602-1_48.

Ma, C., Cao, X., Tong, X., Dai, Q., and Lin, S., 2014, Acquisition of high spatial and spectral resolution video with a hybrid camera system: International Journal of Computer Vision, v. 110, p. 141–155, https://doi.org/10.1007/s11263-013-0690-4.

Maloof, A.C., Porter, S.M., Moore, J.L., Dudás, F.Ö., Bowring, S.A., Higgins, J.A., Fike, D.A., and Eddy, M.P., 2010, The earliest Cambrian record of animals and ocean geochemical change: Geological Society of America Bulletin, v. 122, p. 1731–1774, https://doi.org/10.1130/B30346.1.

Mehra, A., and Maloof, A., 2018, Multiscale approach reveals that *Cloudina* aggregates are detritus and not in situ reef constructions: Proceedings of the National Academy of Sciences, v. 15, no. 11, https://doi.org/10.1073/pnas.1719911115.

Melesse, A.M., Weng, Q., Thenkabail, P.S., and Senay, G.B., 2007, Remote sensing sensors and applications in environmental resources mapping and modelling: Sensors (Basel), v. 7, p. 3209–3241, https://doi.org/10.3390/s7123209.

Neilson, M., and Brockman, G., 1977, The error associated with point-counting: The American Mineralogist, v. 62, p. 1238–1244.

Rogers, A.F., and Kerr, P.F., 1942, Optical Mineralogy: New York, McGraw-Hill.

Shah, A.K., Morrow, R., Pace, M., Harris, M.S., and Doar, W., III, 2021, Mapping critical minerals from the sky: GSA Today, v. 31, https://doi.org/10.1130/GSATG512A.1.

Shand, S., 1916, A recording micrometer for geometrical rock analysis: The Journal of Geology, v. 24, p. 394–404, https://doi.org/10.1086/622346.

Solomon, M., 1963, Counting and sampling errors in modal analysis by point counter: Journal of Petrology, v. 4, p. 367–382, https://doi.org/10.1093/petrology/4.3.367.

Soomro, T.A., Khan, M.A., Gao, J., Khan, T.M., and Paul, M., 2017, Contrast normalization steps for increased sensitivity of a retinal image segmentation method: Signal, Image and Video Processing, v. 11, p. 1509–1517, https://doi.org/10.1007/s11760-017-1114-7.

Tian, Y., Pei, K., Jana, S., and Ray, B., 2018, Deeptest: Automated testing of deep-neural-network-driven autonomous cars: Proceedings of the 40th International Conference on Software Engineering, p. 303–314, https://doi.org/10.1145/3180155.3180220.

Tischlinger, H., and Arratia, G., 2013, Ultraviolet light as a tool for investigating Mesozoic fishes, with a focus on the ichthyofauna of the Solnhofen archipelago, in Arratia, G., Schultze, H.-P., and Wilson, M.V.H., eds., Mesozoic Fishes 5—Global Diversity and Evolution: München, Germany, Verlag Dr. Friedrich Pfeil, p. 549–560.

van den Bergh, J., Chirayath, V., Li, A., Torres-Perez, J.L., and Segal-Rozenhaimer, M., 2021, NeMO-Net—Gamifying 3D labeling of multimodal reference datasets to support automated marine habitat mapping: Frontiers in Marine Science, v. 8, p. 347, https://doi.org/10.3389/fmars.2021.645408.

Yesiloglu-Gultekin, N., Keceli, A.S., Sezer, E.A., Can, A.B., Gokceoglu, C., and Bayhan, H., 2012, A computer program (TSecSoft) to determine mineral percentages using photographs obtained from thin sections: Computers & Geosciences, v. 46, p. 310–316, https://doi.org/10.1016/j.cageo.2012.01.001.